Journal of Materials Chemistry A

ROYAL SOCIETY OF CHEMISTRY

PAPER

View Article Online
View Journal | View Issue

Cite this: J. Mater. Chem. A, 2025, 13, 3034

Characterization and reuse of SiC flakes generated during electrochemical etching of 4H-SiC wafers†

Matteo Barcellona, ‡[a] Vanessa Spanò, ‡[a] Roberto Fiorenza,[a] Salvatore Scirè,[a] Thomas Defforge,[b] Gaël Gautier[b] and Maria Elena Fragalà *[a]

Silicon carbide porous flakes are obtained during electrochemical etching (ECE) of n-doped 4H-SiC wafers. In particular, the use of high current conditions (50–500 mA cm^{-2}) causes detachment of silicon carbide residues from the surface of the etched wafers. Herein, comprehensive material characterization demonstrates the possibility of collecting and using these secondary products of the SiC ECE process. In particular, etching of the two different 4H-SiC faces (Si-face and C-face) results in producing porous flakes, characterized by different structural and chemical properties as investigated using N_2 adsorption isotherms, Scanning Electron Microscopy (SEM), Atomic Force Microscopy (AFM), X-ray Diffraction (XRD), and X-ray Photoelectron Spectroscopy (XPS). Adsorption properties in a water environment were investigated using different classes of dyes (cationic, anionic, and neutral) such as methylene blue, methyl orange, rhodamine B, rhodamine 6G, and thiazolyl blue tetrazolium. The preferential adsorption of the positively charged species well confirms the negative surface charge of the flakes, even though other factors such as steric hindrance and charge screening influence the dye–flake interaction. Methylene Blue (MB) is the most efficiently adsorbed dye and is used as a model to study the adsorption mechanism on both Si and C-face flakes by a thermodynamics and kinetics investigation. The Langmuir model best describes the adsorption mechanism of MB by Si-face generated flakes whilst both Langmuir and Freundlich models fit well the C-face flake adsorption behavior and the kinetic study indicates that the diffusion stage of adsorption is faster than the dye–dye stacking. This preliminary study of the properties of SiC flakes demonstrates their applicability in environmental applications as adsorbent materials whose activity can be mastered by coupling the SiC photocatalytic properties. Moreover, their intrinsic porosity makes possible the dimensional scaling down of these SiC flakes by mechanical sonication to produce SiC nanoparticles as alternative approaches to high-energy ball milling, carbothermic reduction, or laser ablation.

Received 2nd October 2024
Accepted 12th December 2024

DOI: 10.1039/d4ta07035f

rsc.li/materials-a

Introduction

Porous materials are particularly promising from a technological and industrial point of view for a wide range of applications that benefit from the lightness of the materials, the high surface area, the modularity of porosity, and the pore size combined with the specific properties of the constituent materials. These materials therefore have an important role in the ecological transition process that modern society must finalize to ensure a more sustainable future and preserve the health of the earth. In the circular economy, new materials are designed and manufactured so that they can be obtained with manufacturing approaches with high efficiency and low environmental impact both in terms of energy consumption and minimization of the dispersion of waste or secondary products which in any case must be reusable and recyclable rather than being disposed.[1]

Porous materials, classified according to their macro-, meso-, or micro-pore sizes, can be obtained mainly through sintering, foaming methodologies, or approaches that use sacrificial fugitives or replica templates. Noteworthily, most of these approaches require high temperatures (1000–2000 °C) and high-pressure experimental conditions.[2–4] Electrochemical etching (ECE) is a widely used technique that allows working at room temperature and atmospheric pressure, producing porous materials that can be used in various areas of industrial application such as photovoltaics,[5,6] sensors,[7] and biosensors.[6] Porous inorganic materials, among other things, also play an important role in the adsorption of specific analytes and therefore can also be used as active filters for analytical and environmental applications. As regards their use as catalysts, in

[a]University of Catania and INSTM UdR Catania, Department of Chemical Sciences, Viale Andrea Doria, 6, 95125 Catania, Italy. E-mail: me.fragala@unict.it

[b]GREMAN UMR-CNRS 7347, INSA Centre Val de Loire, Université de Tours, Tours, France

† Electronic supplementary information (ESI) available: Morphology, thermodynamics and kinetics features of 4H-SiC flakes. See DOI: https://doi.org/10.1039/d4ta07035f

‡ These authors equally contributed to this work.

addition to porosity, they must be characterized by specific unique chemical–physical properties, such as hardness and mechanical and thermal stability, as well as good chemical inertness and resistance to oxidation. These properties characterize silicon carbide (SiC) which is therefore considered an alternative to many conventional ceramic materials generally used in catalysis. Noteworthily, its semiconductor characteristics make it an interesting alternative to many semiconductor oxides used as photocatalysts.

Herein we provide a comprehensive characterization of porous SiC flakes resulting as "secondary" materials during ECE of 4H-SiC under specific conditions, as illustrated in Fig. 1.

In particular, the high current density ECE on SiC causes the detachment of the flakes which can be collected at the end of the etching procedure. The obtained results demonstrate that the etching of silicon and carbon 4H-SiC faces results in producing flakes characterized by a different morphology and pore distribution as well as surface composition. To our knowledge, the literature does not report examples of porous SiC flakes obtained by ECE of 4H-SiC wafers. Herein, an investigation of the dependence of the flakes' porosity on the nature of the face exposed (Si-face and C-face) to the electrolytic solution is presented.

Of note, the current environmental challenges require urging sustainable technologies for water treatment and hence necessitate the development of innovative solutions that comprise many fields of research from chemistry to physics. Water contamination arises from various sources, including industrial discharges, agricultural runoff, and improper waste disposal. Traditional water treatment methods often fall short in handling emerging contaminants and achieving comprehensive purification: in particular, the use of dyes and pigments in different industries (such as textiles, pharmaceuticals, food, cosmetics, plastics, paints, inks, photographs, and paper) causes the release of colorful wastewater into the environment with consequent serious risks for human health.[8] There are many methodologies used for water purification;[9,10] however, the possibility of manufacturing nanosized materials characterized by high surface-to-volume ratios has made it possible to develop new absorbents (or superabsorbents) capable of removing polluting substances due to non-covalent interactions with the surface of the material. Furthermore, the photocatalytic properties of semiconductor-based nanomaterials have implemented the use of advanced oxidative processes (AOPs) as green methodologies for the abatement of organic pollutants through processes promoted by unspecific and aggressive (super)oxidative radical species (hydroxyl and superoxide radicals) responsible for the complete mineralization of dyes.[11,12]

A preliminary study on the adsorption ability to remove dye molecules from water is herein elucidated. Moreover, we demonstrated the possibility of reusing the porous flakes (instead of their disposal) as reusable adsorbent materials. The adsorption mechanism of SiC flakes has been investigated and the results suggest that the transfer of dye molecules is driven by many factors such as size, shape, and charge of the dye as well as pore size distribution: this latter aspect makes SiC flakes suitable novel adsorbents for the separation of organic dyes. Another important ability of these flakes is related to their complete recyclability and, hence to the possibility of being able to fully restore them without dispersing the material in washing procedures.

Since porous silicon carbide (SiC) is emerging as a promising material to be used in photocatalysis[13] due to an appropriate band-gap (varying from 2.4 to 3.4 eV) and its remarkable physical properties and chemical stabilities, the obtained results are important from the perspective of using porous SiC flakes as a multifunctional material to achieve more efficient removal of dyes from wastewater by coupling its absorbent properties to the photocatalytic activity.[14]

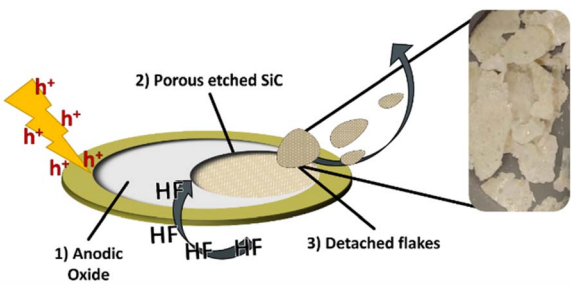

Fig. 1 Mechanism of SiC flake formation during SiC ECE treatment. The SiC substrate is supplied with a voltage that causes surface oxidation (point 1). The anodic oxide is etched by HF in the electrolytic solution (point 2). The flakes detach from the SiC etched surface due to the high current densities (point 3).

Materials and methods

4H-SiC flake fabrication

4H-SiC flakes were produced through the electrochemical etching (ECE) technique using a 6-inch homemade PS electrochemical cell, specifically designed for collecting particles from high-area wafers. The electrochemical attack was executed in galvanostatic mode, involving 300 etching cycles with pulsed current at 510 mA cm^{-2}. The ECE attack was conducted with a pulse of 2 s interspersed with a pause of 5 s. The electrolyte solution comprised a mixture of HF 30 wt%, CH_3COOH (acetic acid) 10 wt%, and H_2O. CH_3COOH has the role of achieving homogeneous pores along the etching direction.[15] SiC flake fabrication was performed at room temperature and atmospheric pressure. A 4-inch 4H-SiC n-type material with a resistivity of 0.037 Ω cm was chosen for the top-down approach. Ti/Ni metallization was performed on the wafer periphery in order to ensure a good ohmic contact during the anodization. Flakes were obtained by selectively etching the C-face or Si-face of the wafer. Prior to their collection, the flakes were washed multiple times in DI water to eliminate adsorbed HF until the detection of neutral pH conditions. The dispersed flakes were filtered and dried in an oven at 80 °C for 4 hours. Approximately 1 g of flakes was obtained for each wafer.

Investigation methods

SEM micrographs were acquired using an FE-SEM instrument (Jeol JSM-7900F). A typical probe energy of 10 kV was set for the

image acquisition. An in-lens detector (UED) and a working distance of 4 mm were standard settings to acquire high-magnification images. A minimum chamber pressure of 3×10^{-3} Pa was employed during the analysis. The flakes were deposited on a carbon tape film randomly distributed in order to ensure the morphological characterization of both the top surface and the sidewalls at once.

Atomic Force Microscopy (AFM) was employed to characterize the surface roughness in this study. Measurements were conducted using an NT-MDT modular AFM NTEGRA instrument featuring a PX Ultra controller system. The instrument utilized a high-resolution silicon tip (ETALON HA_NC type) with specifications including a resonant frequency of 140 kHz ± 10%, a force constant of 3.5 N m^{-1} ± 20%, a cantilever length of 124 μm ± 2 μm, a cantilever width of 34 μm ± 3 μm, and a cantilever thickness of 1.85 μm ± 0.15 μm. Imaging was performed in semi-contact mode at room temperature and atmospheric pressure.

Rugosity parameters were assessed using Root Mean Square (RMS) and Roughness Average (RA). The Peak-to-Peak (PtP) parameter represented the maximum height in the acquisition. The S_m parameter quantified the average lateral distance between peaks in a section, expressed in nm or μm.

Elemental and chemical investigations were conducted utilizing the X-ray Photoelectron Spectroscopy (XPS) characterization technique. The analysis was specifically carried out with a PHI 5000 VersaProbe II, set at a take-off angle of 45° relative to the sample surface holder. The X-ray source was an Al Kα (1486.6 eV), with a pass energy of 187.85 eV for the survey scans and 23.5 eV for the detailed scans. The base pressure within the chamber was maintained at 1×10^{-8} Pa. Spectral calibration was performed by setting the C 1s signal of adventitious carbon at 285.0 eV. Peak intensities were determined prior to the removal of Shirley's background, followed by the calculation of elemental percentages based on the sensitivity factors reported in the referenced scientific literature.[16] The deconvolution process was executed using the XPSPeak 4.1 software.[17]

The crystallinity of 4H-SiC flakes was investigated by the X-ray Diffraction (XRD) technique employing a Rigaku SmartLab instrument. The analysis was conducted in θ–2θ geometry using a Cu Kα source.

The porosity of the flakes was assessed with adsorption–desorption measurements of N_2 at −196 °C using a Micromeritics Tristar 3000 instrument. The surface area was determined with the Brunauer–Emmett–Teller (BET) methodology, whereas the pore size distribution with the Barrett–Joyner–Halenda (BJH) model.

The materials were pre-treated before the measurements by out-gassing at 100 °C overnight.

Adsorption experiments

The adsorption experiments were done following the decrement of the concentration in a 5 mL aqueous solution of the dyes. The Methylene Blue (MB) molecule was used as a model to investigate the adsorption capacity of 4H-SiC flakes. The decrement of MB concentration was followed by UV-vis spectroscopy (Jasco V-530). The MB chloride dye salt ($M_w = 319.85$ g mol^{-1}) absorbs the light in the visible region with a peak at 664 nm. Thermodynamics and kinetics studies of the MB adsorption on the 4H-SiC flake surface were done following the q_t (mg g^{-1}) curve as a function of time. The q_t factor expresses the milligrams of dye adsorbed per gram of adsorbent. The q_t is obtained as follows:

$$q_t(\text{mg g}^{-1}) = \frac{(A_0 - A_t)\cdot V \cdot M_w \cdot 1000}{\varepsilon_{664}\cdot b \cdot m_{ads}}$$

where A is the UV-vis absorbance, V is the volume of MB solution (L), M_w is the MB molar mass (g mol^{-1}), ε_{664} is the UV-vis MB extinction coefficient at 664 nm (L mol^{-1} cm^{-1}), b is the cuvette optical path (cm), and m_{ads} is the adsorbent mass (g). The extinction coefficient at 664 nm (ε_{664}) was experimentally determined and was equal to 9.5×10^4 L mol^{-1} cm^{-1} at pH = 7. The calibration linear fit is shown in Fig. S1.†

The relevant value of the isotherm adsorption curve is the q_e (mg g^{-1}) which is the q_t value at the equilibrium state at each dye concentration. Methylene blue concentrations of 7, 10, 15, 20, and 30 mol L^{-1} were used for the experiments at pH = 7. The isotherm experiments were executed at a temperature of 298.15 K. The adsorbent mass at each experiment was 2 mg.

The 4H-SiC flake adsorption potential was investigated also employing the dyes methyl oange ($M_w = 327.33$ g mol^{-1}), rhodamine B chloride salt ($M_w = 479.02$ g mol^{-1}), rhodamine 6G chloride salt ($M_w = 479.02$ g mol^{-1}) and thiazolyl blue tetrazolium bromide salt ($M_w = 414.32$ g mol^{-1}). The molecular structures and their properties were obtained using Avogadro free software.

After each adsorption cycle, the flakes were recovered by 70 wt% HNO_3 treatment. The HNO_3 was then eliminated by heating at 80 °C until complete evaporation of the solution.

Results and discussion

4H-SiC flake characterization

The production of 4H-SiC flakes was done by the ECE technique. Two different experiments were conducted by keeping constant the ECE parameters (current density, pulse, duration, and electrolytic solution composition) and by varying the 4H-SiC face exposed to the electrolytic solution. Namely, flakes from the Si-face and C-face were obtained. The two 4H-SiC faces led to different flake morphologies due to the different preferential lattice plane etching. The 4H-SiC Si-face-derived flakes exhibit a cauliflower-like morphology (Fig. 2a) on top and a dendrimeric morphology (Fig. 2b) on the sidewall as already reported in the scientific literature.[18] However, the C-face derived flakes show a columnar-like morphology on both the top (Fig. 2c) and sidewall (Fig. 2d) sections.

The morphology of Si-face flakes is due to the pores' propagation along the $(11\bar{0}4)$ and $(1\bar{1}04)$ planes[19] with angles between 90 and 120°. The remarkable adaptability of the ECE approach can be attributed to its ability to yield diverse morphologies on the Si-face, as explained by Shishkin and colleagues.[18] However, the well-known C-face flakes' columnar morphology[20] is attributed to the preferential etching in the [0001] direction.[21,22]

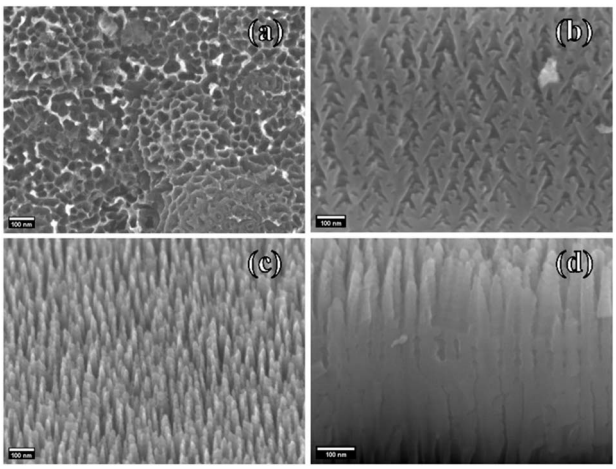

Fig. 2 SEM micrographs of Si-face 4H-SiC flakes (a) top view and (b) sidewall view, and C-face SiC flakes (c) top view and (d) sidewall view.

Moreover, the use of pulses instead of constant current densities leads to homogeneous morphology in-depth and narrow pore distribution in the flakes as mentioned in a previous study.[23] The morphological differences between the two 4H-SiC faces are further elucidated by AFM analysis. The 2D 4 μm^2 acquisition of the Si-face (Fig. S2a†) and C-face (Fig. S2b†) reveals the surface morphology as seen in Fig. 2a and b: the micrometric flatness of Si-face flakes (see Fig. S2c†) compared to C-face flakes (see the wave-like structure in Fig. S2d†) is confirmed by the different AFM scanning area (4, 25, and 100 μm^2) measurements. The AFM parameters reported in Table 1 show Si-face flakes' constant values of the typical roughness parameters, namely RMS, RA, and PtP, by decreasing the scan area. Otherwise, the C-face flakes show a decreasing trend of the cited parameters as the scan area was decreased, due to the wave-like shape.

The cause of the wavelike shape of the C-face flakes has not been already uncovered. One may assume that the starting morphology of the C-face 4H-SiC wafer, which is characterized by terraces, imprints the wave morphology as observable in Fig. S2d.† The presence of terraces on the C-face is due to the 8° offset typical of 4H-SiC wafers.[24,25] The C-faces generally lack polishing treatments, and the terraces are still visible.

XPS analyses show no relevant differences in terms of elemental composition for the two 4H-SiC surfaces, as shown in Table S1:† the Si-face flakes are distinguished by a slightly lower Si content and slightly higher oxygen content than the initial wafer material whilst the C-face flakes have a lower oxygen content. The C 1s photoelectron peak reported in Fig. 3a shows two main components attributed to Si–C, at binding energy (BE) of 283.4 eV[26] and C–C at 284.8 eV[27] (the C–C is due to adventitious carbon contamination) on both the Si-face and C-face. However, a specific Si–O–C component at 286.6 eV[27,28] is observed for the C-face, which contrasts with the well-defined C–O group at 286.2 eV[27] for the Si-face. The C1s spectra of the C-face flakes exhibit a more defined tail at high BE (attributed to carboxy moieties) than the Si-face flakes. The presence of the Si–O–C group on the C-face surface is supported by a component in the Si2p signal (Fig. 3b) at BE 102.4 eV.[29] The Si–C bond is detected in both Si-face and C-face flake surfaces at 101.3 eV.[26]

Table 1 AFM roughness parameters of Si-face and C-face 4H-SiC flakes on 4, 25, and 100 μm^2 scan area. Root Mean Square (RMS), Roughness Average (RA), and Peak to Peak (PtP)

	Acquisition area	RMS (nm)	RA (nm)	PtP (nm)
4H-SiC Si-face	100 μm^2	16.0	12.5	170.7
	25 μm^2	16.0	12.6	123.8
	4 μm^2	14.3	11.2	120.9
4H-SiC C-face	100 μm^2	126.8	98.1	951.8
	25 μm^2	50.5	40.7	416.9
	4 μm^2	14.6	11.8	91.2

The main surface chemical difference lies in the absence of the Si–O–C group on Si-face flakes with respect to the C-face flakes. It is well-known that the Si–O–C moiety formation occurs during the oxidation treatment of the SiC surface.[28,30,31] It is noted that surface oxidation is easily achieved on the 4H-SiC C-face rather than the Si-face. The reason behind this could be attributed to the flatter surface of the Si-face than the C-face which causes an increase in the oxidation activation energy.[32] Furthermore, the formation of Si–O–C as a preliminary layer was detected during the transition of SiC into SiO_2 in carbon-rich layers which is typical of the C-face side.[33]

The lower oxygen content of C-face flakes (see Table S1†) and the presence of the SiO_2 moiety on the Si-face flakes' surface suggest that the Si–O–C acts as a passivation group toward further oxidation of the SiC flake surface when exposed to air.

Despite the carving process conducted by electrochemical etching on the starting 4H-SiC wafer, the resulting flakes preserve the crystallinity as shown in the XRD pattern of Fig. 3c. One sharp signal at 35.6° was detected and it is attributed to the (004) planes.[34,35] The electric properties of 4H-SiC flakes reflect the saved crystallinity. The application of 4H-SiC flakes in photocatalysis requires the WBG properties of the starting material. The application of 4H-SiC flakes in Advanced Oxidation Processes (AOPs) will be discussed later.

The XPS analysis sheds light on the possible surface terminations of the flakes starting from the two different faces of SiC. The different terminations could in principle answer to chemical groups of molecules in the water environment for molecular sieves and filters. The adsorption mechanism starts with the recruitment of molecules towards the surface of the adsorbent material. The flow of molecules to the surface is driven by diffusion and electrostatic forces. The 4H-SiC surface is negatively charged due to dangling oxygen bonds on it, which are available on both Si-face and C-face flakes.

If the adsorption starts with molecule recruitment, a highly porous material is obviously more efficient in the adsorption capacity than a low porosity one. The differences in porosity between the two sets of flakes can be rationalized by the different morphology of the flakes. As previously anticipated, the Si-face flakes are characterized by dendrimeric structures on the sidewalls and a cauliflower-like morphology on top. However, the C-face flakes are characterized by a columnar-like

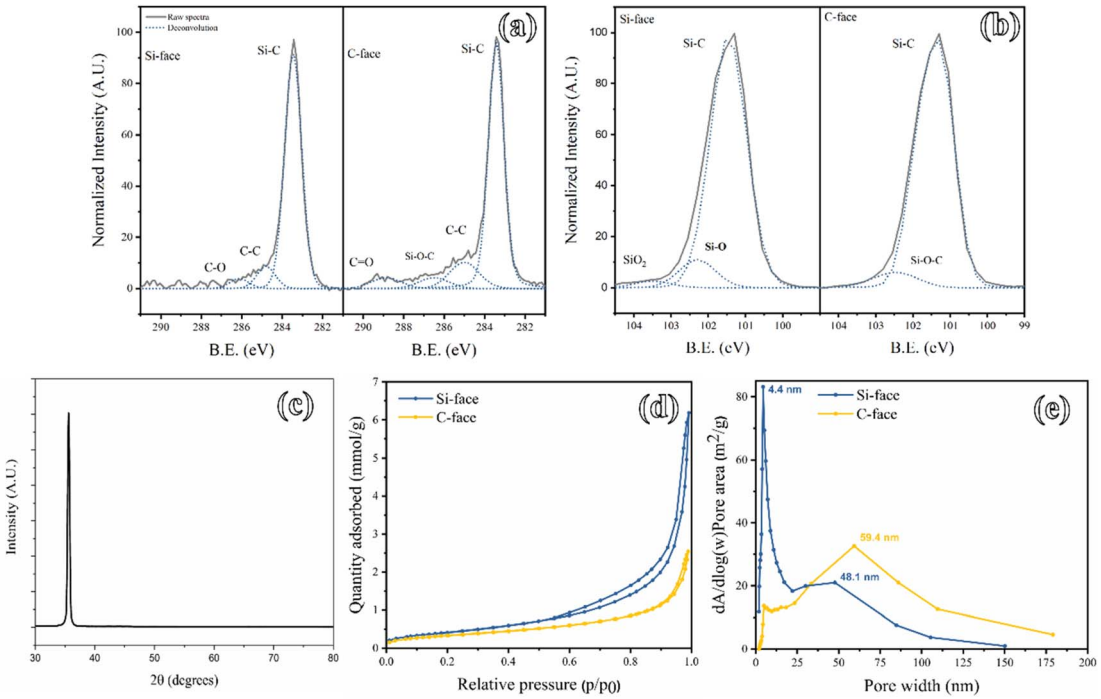

Fig. 3 XPS spectra of 4H-SiC flakes fabricated from the Si-face (left) and C-face (right) of (a) C 1s and (b) Si 2p photoelectron signals. Deconvolution components are displayed as blue dotted curves under the experimental spectra in light gray lines. (c) $\theta-2\theta$ geometry XRD pattern of 4H-SiC Si-face flakes. (d) N_2 physisorption curves of 4H-SiC flakes from the Si-face (blue plot) and C-face (yellow plot) and (e) BJH (desorption curve) pore size distribution of 4H-SiC flakes from the Si-face (blue plot) and C-face (yellow plot).

morphology. Comparing the two morphologies, it is possible to note the presence of smaller pores in the Si-face than in the C-face ones.

An ImageJ analysis using a threshold tool on SEM micrographs (see Fig. S3†) revealed and confirmed the higher surface area of Si-face flakes than C-face-derived ones. In particular, the Si-face flakes present a porosity of 45% ± 12% and 44% ± 5% respectively in the sidewall and in the plane portion of the flakes. The C-face flakes with values of 21% ± 5% and 30% ± 6% of the sidewall and plane portion, respectively, were for the most part lower than the corresponding values for the Si-face flakes.

The porosity of 4H-SiC flakes was determined by N_2 physisorption measurements. The N_2 isotherms of the examined samples (Fig. 3d) showed a type III curve with a H3 hysteresis, more evident for the Si-face and typical of slit-shaped pores.[36] The Si-face allowed a higher amount of N_2 adsorption and consequently, it showed a higher BET surface area (46.5 $m^2\ g^{-1}$) compared to the 36.4 $m^2\ g^{-1}$ of the C-face.

The BJH pore size distribution of the fabricated flakes is shown in Fig. 3e. The blue curve of Fig. 3e shows the pore size distribution of the Si-face derived flakes characterized by a bimodal curve of mesopores with two peaks at 4.4 nm and 48.1 nm. On the other hand, the C-face flakes (yellow plot of Fig. 3e) show a pore size distribution curve shifted towards larger pores with a maximum peak at 59.4 nm, in the macropore range. These changes in the pore width explain the different surface areas of the samples: in particular, the Si-face flakes, characterized by a narrower pore size distribution, exhibit a higher surface area than the C-face counterpart.

The role played by current and HF concentration during the ECE process of both SiC faces influences the pore size distribution as well as the surface area of the flakes, as demonstrated by preliminary experiments reported in Table S2.†

These changes in the pore width are strictly connected with the surface area of the samples with the Si-face derived flakes, owing to a narrower pore size distribution, exhibited a higher surface area than the C-face counterpart. Considering that the commercially available SiC nanoparticles are characterized by BET surface area values of 5–15 $m^2\ g^{-1}$,[37–40] it is possible to note how the peculiar preparation method, here proposed, allowed the fabrication of 4H-SiC flakes with meso- and macro-porosity and an increased surface area.

Although the SEM and BET analyses were useful in understanding the differences in porosity between the two sets of flakes, neither the morphological nor the textural analysis can unveil the real behavior of molecule adsorption in a water medium. For this purpose, thermodynamics and kinetics experiments were executed.

Dye adsorption: thermodynamics and kinetics investigation

The adsorption process is driven by a thermodynamic propensity of interaction *via* secondary bonds between the molecules and the surface of the adsorbent material. At the same level as the thermodynamics investigation, the kinetic aspects of adsorption are of utmost importance. Methylene Blue (MB) is a cationic dye (see the structure in Fig. S11a†) used as a model

structure to perform adsorption isotherm experiments. It has an absorption peak at 664 nm which is the reference of dye concentration: following the decrement in concentration and converting it in q_t value, it was possible to investigate the adsorption features of the coupled 4H-SiC flakes and MB.

Thermodynamics and kinetics investigation were done following the isotherm curves recorded at a temperature of 298.15 K, as shown in Fig. 4. A total of 5 MB concentrations (7, 10, 15, 20, and 30 μM) were chosen to perform adsorption isotherm experiments. In particular, the experiments were performed on both Si-face (Fig. 4a) and C-face (Fig. 4b) derived 4H-SiC flakes.

Around 200 min, all the experiments reached the equilibrium state of adsorption where the concentration remained constant.

Isotherm adsorption curves in Fig. 4 exhibit an L-shape which is typical of molecule adsorption on a solid/liquid interface.[41] As evidenced in Fig. 4, the MB adsorption in Si-face flakes is higher than in the C-face. The isotherm experimental results in the water environment confirm the textural properties of the samples, with the 4H-SiC Si-face flakes showing a higher specific surface area (46.5 $m^2\ g^{-1}$) than C-face flakes (36.4 $m^2\ g^{-1}$).

Different adsorption isotherm thermodynamic models were formulated[42] although the two most practical are the Langmuir and Freundlich models.[43,44] The Langmuir isotherm model is essential to understand the adsorption processes in surface chemistry. It considers various crucial components, such as

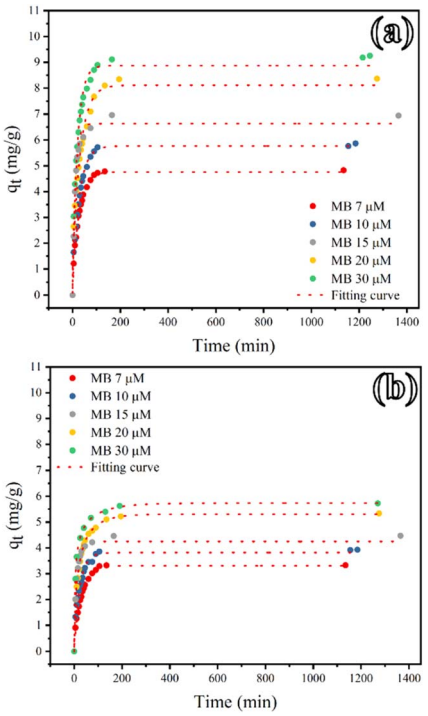

Fig. 4 Adsorption isotherm of MB ($T = 298.15$ K, $[MB]_0 = 7$, 10, 15, 20, and 30 μM) reported as q_t value variation over time for 4H-SiC flakes (a) Si-face and (b) C-face. The fitting curves are shown as dashed red lines.

assuming a uniform surface with identical adsorption sites. Moreover, it incorporates the concept of monolayer adsorption, which means that once a site is occupied, no additional adsorption can occur.[45,46] The Langmuir's model is described using the following equation:

$$\frac{C_{eq}}{q_{eq}} = \frac{1}{K_L\, Q_m} + \frac{C_{eq}}{Q_m}$$

where C_{eq} is the concentration at the equilibrium (mg L^{-1}), q_{eq} is the mass of dye per gram of adsorbent (mg g^{-1}), Q_m is the maximum adsorption capacity (mg g^{-1}), and K_L is the Langmuir constant (L mg^{-1}).

The heterogeneous adsorbent surfaces are best described using the Freundlich isotherm model. This model reveals that the adsorption process is not consistent throughout the entire surface of the adsorbent. It is a practical theory that finds application when the solutes attach to solid material in a non-linear way.[47] Freundlich's isotherm model is described using the following equation:

$$\ln(q_{eq}) = \ln(K_F) + \frac{1}{n}\ln(C_{eq})$$

where C_{eq} is the concentration at the equilibrium (mg L^{-1}), q_{eq} is the mass of dye per gram of adsorbent (mg g^{-1}), and K_F is the Freundlich constant which expresses the adsorption capacity, and n is an empirical constant of adsorption intensity.

Freundlich's linear fit graphs are shown in Fig. S4† whereas Langmuir's linear fit graphs are shown in Fig. S5.† The fundamental parameters of Freundlich (K_F and n) and Langmuir (K_L and Q_m) models, associated with the coefficient of determination (R^2) values of each fitting, are reported in Table 2. The pore size (see Fig. 3e) and specific surface area determined by BET analysis reflect the thermodynamics fit parameters of both Freundlich and Langmuir models. Freundlich's adsorption isotherm model fits less well than the Langmuir model (see R^2 values of Table 2). As previously stated, this result indicates a homogeneous adsorption mechanism of a dye's monolayer over the surface of the adsorbent material, which is typical of nanocrystalline cellulose[48] and Metal–Organic Frameworks (MOFs),[49,50] distinguished by ordered structures. According to the Langmuir isotherm adsorption model, the maximum capacities of the Si-face and C-face flakes are respectively 7.23 mg g^{-1} and 5.96 mg g^{-1}: the slightly higher adsorption capacity of the 4H-SiC flakes is attributed to the porosity of the Si-face flakes being higher than that of C-face flakes.

The kinetics investigation was conducted by applying two models: the pseudo-first-order model (Lagergren model) and the pseudo-second-order model. According to the former, as described in the following equation, the rate of adsorption is proportional to the number of unoccupied sites:[51]

$$\ln(q_{eq} - q_t) = \frac{K_{pf}\, t}{2.303} + \ln(q_{eq})$$

where q_{eq} (mg g^{-1}) is the mass of adsorbed dye at equilibrium per mass of absorbent, q_t (mg g^{-1}) is the equivalent q (mg g^{-1}) value at a certain time, K_{pf} (min^{-1}) is the pseudo-first-order rate constant, and t is the time (min).

Table 2 Freundlich and Langmuir fitting parameters of MB isotherm adsorption at 298.15 K on 4H-SiC Si-face and C-face flakes

Samples	Freundlich's model	R^2	Langmuir's model K_L (L mg^{-1}), Q_m (mg g^{-1})	R^2
4H-SiC Si-face flakes	$K_F = 5.27$ $n = 5.78$	0.61	$K_L = 3.95$ $Q_m = 7.23$	0.99
4H-SiC C-face flakes	$K_F = 2.98$ $n = 3.86$	0.86	$K_L = 0.72$ $Q_m = 5.96$	0.99

The applied model is not in good accordance with the experimental data, as displayed in Fig. S6† and indicated by the low R^2 values in Table 2.

The pseudo-second-order model considers the adsorption rate dependent on the square of the number of unoccupied sites,[51] as described using the following equation:

$$\frac{t}{q_t} = \frac{t}{q_{eq}} + \frac{1}{K_{ps} q_{eq}^2}$$

where q_{eq} (mg g^{-1}) is the mass of adsorbed dye at equilibrium per mass of absorbent, q_t (mg g^{-1}) is the equivalent q (mg g^{-1}) value at a certain time, t is the time (min), and K_{ps} is the pseudo-second-order rate constant (g mg^{-1} min^{-1}).

As evident from Fig. S7† and Table 2, the pseudo-second-order model fits even better than the pseudo-first-order experimental data for both Si-face and C-face flakes.[52]

Finally, Weber's intraparticle diffusion model is the last model applied for the kinetics investigation of MB adsorption on 4H-SiC flakes, as shown in the following equation:

$$q_t = K_i t^{1/2} + q_c$$

where q_t (mg g^{-1}) is the equivalent q (mg g^{-1}) value at a certain time, q_c (mg g^{-1}) is the y-value intersection point of the second adsorption step, t is the time (min), and K_i is the intraparticle diffusion rate constant (mg g^{-1} min$^{-1/2}$) of each adsorption stage.

The plot in Fig. S8† was fitted according to a piecewise linear regression model: the first linear section describes the initial and fastest step (K_1, high value of slope) of dye adsorption, with the formation of a monolayer, on the adsorbent surface. This step is driven by the diffusion force of the dye from the solution (high concentration) to the adsorbent surface (low concentration). The slope associated with the second section (K_2) is lower than that of the first step and represents the stage of dye–dye stacking on top of the adsorbent surface.[52,53] The piecewise regression was a good model to describe more in-depth the diffusion driving force and the MB stacking tendency. Generally, in both Si-face and C-face flakes, the K_1 values are one order of magnitude higher than K_2, thus indicating that the diffusion stage of adsorption is faster than the dye–dye stacking, and mostly includes the majority of the dye adsorption. The kinetics parameters of each model for 4H-SiC Si-face and C-face flakes are listed in Table S3† and point to faster kinetics of MB adsorption on Si-face flakes than on C-face flakes.

4H-SiC flakes as molecular sieves

The complex porous structure of 4H-SiC flakes should in principle guarantee selectivity against different classes of organic dyes. Molecules' features such as size, charges, steric hindrances, and acid–base characteristics differentiate the molecules taken under study in this work. In particular, electrostatic interactions between the 4H-SiC porous flakes and differently charged and neutral dyes are herein scrutinized. In particular, other than MB, Rhodamine B (RhB), Thiazolyl Blue Tetrazolium (TBT), and Methyl orange (MO), whose main properties are reported in Table S4,† have been tested. The molecular structure of these dyes is shown in Fig. S11.†

Generally, an adsorption process is mainly influenced by critical factors such as the size of the adsorbent pores, the surface-active groups' acidity, the steric hindrance of the molecules as well as the charged group acidity.[54,55] All the molecular systems under investigation have a similar length (between 1.1 and 1.3 nm) fully compatible with the pores size of both Si-face and C-face flakes and, accordingly, their size and steric hindrance should not affect adsorption selectivity.

The role of the dyes' charges is elucidated by testing the flakes's adsorption capacity of the anionic MO (30 μM solution) at two different pH values. The pK_a value of the –SO_3 group is 3.5,[56] thus it is possible to work with negative and neutral MO by working at pH = 7 (negatively charged) and pH = 1 (neutral). In both cases, the adsorption percentage is very low (~2%) for both Si-face and C-face flakes. The MO experiments at pH = 1 suggest the absence of any hydrophobic interaction, while the test at pH = 7 confirms the negatively charged surface of SiC flakes.

The cationic MB was taken as a model molecule for the thermodynamics and kinetics investigation of 4H-SiC flakes (resulting from ECE of both Si- and C- 4H SiC wafer face). At pH = 7 (after 200 min), a MB adsorption of 49% for Si-face and 31% for the C-face points to an electrostatically driven affinity of the flakes towards cationic dyes. This behavior is furthermore confirmed by testing model anionic and cationic porphyrin having similar size and shape: in particular, the tetra-cationic *meso*-tetrakis(*N*-methylpyridinium-4-yl)porphyrin (H_2T_4) was adsorbed by SiC flakes (~40%) while no adsorption was detected for the anionic *meso*-tetra(4-sulfonate phenyl)porphyrin (H_2TPPS) porphyrin (data not shown). However, by testing other cationic molecules having a different structure such as RhB and TBT, a lower adsorption is achieved on both Si-face and C-face flakes with respect to MB. Fig. 5a summarizes the adsorption tests done on the selection of dyes described in Table S4.† These data highlight the role of the electrostatic repulsion between the negatively charged MO and porous SiC. Noteworthily, although the a-SiC and 3C-SiC can acquire a positively charged surface at a pH value below 4.5,[57,58] the surface of 4H-SiC remains negatively charged within the pH range of 0 to 14.[59] Therefore, the

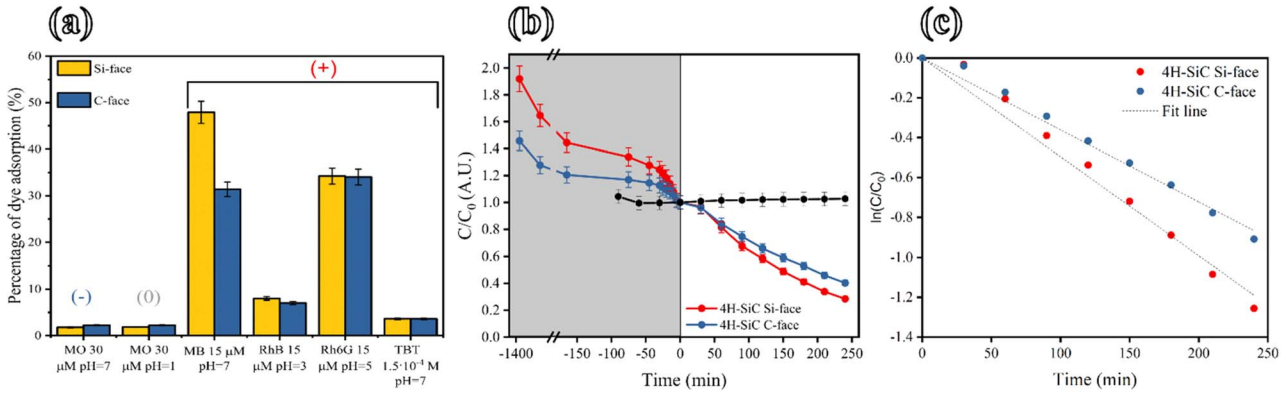

Fig. 5 (a) Bar graph of dye adsorption percentage of MO 30 μM at pH = 7, MO 30 μM at pH = 1, MB 15 μM at pH = 7, RhB 15 μM at pH = 3, Rh6G 15 μM at pH = 5 and TBT 1.5 × 10^{-4} M at pH = 7 on 4H-SiC Si-face (yellow bars) and C-face (blue bars) flakes. The investigated dyes are grouped by their negatively, neutral, and positively charged groups. (b) Adsorption and photocatalytic degradation curve of MB 15 μM. The experiments were conducted with 4H-SiC Si-face (red curve) and C-face (blue curve) flakes. The adsorption experiment was conducted under dark conditions (grey section of the graph) until SiC flake saturation. Photolysis of MB is shown as a black curve. (c) Pseudo-first order kinetics of MB 15 μM photocatalysis by 4H-SiC Si-face (red dots) and C-face (blue dots) flakes.

negative surface charge of porous flakes is in good agreement with the affinity with MB, which is efficiently adsorbed by both Si-face and C-face flakes (Fig. 5a). However, the electrostatic force cannot be the only driving force that regulates dye adsorption as pointed out by the flakes' interaction with RhB. This dye is, in fact, positively charged at pH = 3, but it is faintly adsorbed by both Si-face and C-face flakes showing an adsorption percentage of 8% and 7%, respectively (Fig. 5a). Mass transfer inside porous materials is influenced and limited by many factors overcoming a favorable coulombic interaction, such as pore narrowing, steric hindrance of dyes, and interaction/aggregation between dye molecules.[60] Accordingly, RhB has a higher steric hindrance around the positive charge (see Fig. S11b†) represented by the presence of two ethyl groups rather than the methyl groups of MBs. This hypothesis is supported by the adsorption behavior of Rh6G on 4H-SiC flakes (see Fig. 5a): in this case, adsorption percentages of 34.2% and 34% respectively for Si-face and C-face flakes have been measured. Of note, the Rh6G has only one ethyl group bonded to the positively charged nitrogen (see the molecular structure in Fig. S11c†): this implies a lower steric hindrance around the positive charge than the RhB molecule. However, the observed behavior well matches the role of electron donor substituents that reduce the electron density around positively charged nitrogen, thus reducing the interaction with flakes.

Finally, the TBT molecule was also poorly adsorbed by flakes (3.6% on C-face flakes and 0.2% on C-face flakes): in this case, the steric hindrance of the molecular structure can be responsible for this difference with respect to MB and Rh6G (Fig. S11d†). TBT has a fixed positive charge that does not depend on the pH value, but its access inside the pores is limited by the hindrance of the chemical groups around the charged atom causing minor efficient recruitment of molecules to the surface of the flakes. Observing the overall results of all the cationic dyes, one may note that the difference in adsorption percentage decreases between Si-face and C-face by increasing the steric hindrance of the dyes. The effect is reasonably attributed to the major role of macropores on both Si-face and C-face flakes of dye molecules with high steric hindrance.

4H-SiC flakes as a photocatalyst

In the previous section, we discussed the possibility of removing organic pollutants from water streams by exploiting the porosity of 4H-SiC flakes. Another possible strategy for organic pollutant removal from water is by employing AOPs, exploiting the 4H-SiC WBG semiconductor properties. The photocatalytic degradation of organic pollutants in water leads to the mineralization into CO_2 and H_2O.[61–63] The 4H-SiC is a Wide Band Gap (WBG) material with a band-gap value of 3.2 eV. The morphology and crystallinity characterization demonstrates that the 4H-SiC flakes preserved the properties of the starting material after their fabrication by the ECE technique. The semiconductor properties leave room for photocatalytic applications. Herein, photocatalysis experiments using 4H-SiC flakes were conducted. The MB dye was chosen as a model of organic pollutants in water. The flakes were immersed in a 15 μM solution of MB. The solution was kept in the dark for 24 h as a starting adsorption delay time prior to the photocatalysis start. The C_0 matches the solution molar concentration after SiC flake saturation, corresponding to the beginning of the photocatalysis phase. The solution and the flakes were irradiated by using a 365 nm UV lamp for 240 min as shown in Fig. 5b. The photolysis of MB, in the absence of flakes, is negligible as shown by the black curve in Fig. 5b.

The experimental curves were best fitted with the pseudo-first-order kinetics model (see Fig. 5c). It was possible to calculate the degradation constant values of 4.96 × 10^{-3} min^{-1} and 3.61 × 10^{-3} min^{-1} for Si-face and C-face flakes, respectively. In both cases, the linear best-fit R^2 value is 0.99. The slightly higher photocatalytic efficiency of Si-face flakes over C-face flakes is due to the higher porosity of the former. The photocatalysis mechanism occurs on the very near photocatalyst surface. Hence, a higher surface area is beneficial over the photocatalyst efficiency.

4H-SiC flake recovery

One of the peculiarities of SiC flakes relies on the possibility of recovering and reusing them after the dye adsorption saturation. SiC flake recovery after MB saturation can be followed by a Sodium Dodecyl Sulfate (SDS) 5 wt% solution desorption treatment. The Methylene Blue (MB) stripping from the SiC flake surface by SDS is carried out by the formation of micelles and by hydrophobic/hydrophilic interactions occurring when the concentration of surfactants in water exceeds the Critical Micellar Concentration (CMC). In fact, micelles possess a hydrophobic core in a water environment that can encapsulate organic compounds.[64,65] The electrostatic interaction between the positively charged MB and the porous material surface is weakened by the presence of SDS, which could cause the desorption of the dye.[66] MB stripping from SiC flakes with SDS was corroborated by UV-vis spectroscopy: the spectrum of desorbed solution shows a peak shift of the monomeric form of MB from 664 nm to 619 nm due to MB interaction with SDS, as shown in Fig. S9.† As elucidated in Fig. S9a† the Si-face flakes release less MB when compared to C-face flakes (see Fig. S9b†) and this difference is explained by considering the pores size distribution of the two flake systems (see Fig. 3b). However, the MB stripping with SDS is not highly efficient since after 90 min the solution is saturated with MB and no further dye is removed from the flakes (see Fig. S9†). For this reason, another approach to SiC flake recovery after an adsorption cycle consists of dipping them in a hot solution of concentrated HNO_3 (70 wt%): in this case, the strong oxidation properties of HNO_3 ensure the complete removal of desorbed MB (completely mineralized into CO_2 and H_2O). In fact, as soon as the MB starts to desorbs out of the flakes' pores the solution changes color from blue to pale violet before turning uncolored: this intermediate color is associated with the conversion into thionin (Lauth's violet) in oxidant and/or acidic solutions.[67] The combination of strong oxidants in an acidic solution as well as the solution temperature (herein 80 °C) promotes the final complete mineralization of MB.[68]

Noteworthily, the observed discoloration is not due to the conversion into the leuco-form since HNO_3 represses any possible reduction mechanisms in the solution.[69,70] This treatment is able to completely restore the flakes to their original conditions as well evident in the bar chart reported in Fig. S10†: the maximum percentage of MB adsorption achieved for pristine SiC flakes was recovered after the treatment in HNO_3 solution. This result highlights two important aspects: (i) the HNO_3 washing is efficient in eliminating all the dye adsorbed in the whole material and (ii) the SiC flakes retain the chemical inertness of SiC wafers, even after the electrochemical etching. Noteworthily, the use of hot and concentrated HNO_3 solution to restore an adsorbent material saturated with a dye cannot be applied to the most used ceramic or polymeric materials, which are susceptible to the chemical environment exhibiting coagulation and dissolution phenomena.[71–73]

Conclusions

Porous SiC flakes were produced as waste materials during the electrochemical etching of highly doped 4H-SiC wafers: depending on the SiC face exposed to the electrochemical bath, the obtained Si-face and C-face flakes are characterized by a different porosity as well as pore size distribution. In particular, SiC flakes obtained by Si-face etching possess micropores, with a size of about 4 nm, that are not present in the counterpart generated by etching the C-face. In addition, mesopores of about 50–60 nm are present in both C-face and Si-face flakes. The XPS analysis confirms a similar surface composition and the presence of oxidized moieties drives the selectivity of the adsorption process of dyes in solution. In fact, SiC flakes efficiently adsorb positively charged methylene blue, whilst the negatively charged methyl orange remains in solution, in good agreement with literature data that report on the negative surface charge of SiC.[59] The different pore distribution of C-face and Si-face flakes affects the MB adsorption mechanism: a Langmuir model well fits the behavior of Si-face flakes whilst no preferential fitting is applicable to C-face counterparts. Adsorption capacities of 7.23 mg g^{-1} and 5.96 mg g^{-1} respectively of Si-face and C-face flakes were calculated from isotherm adsorption experiments. The differences in adsorption capacity values are attributable to the divergence in pore size distribution between the two sets of flakes. Of note, the adsorption is ineffective on positively charged dyes, such as rhodamine B or thiazolyl blue tetrazolium, and this behavior is attributed to the dye structure and to the steric hindrance and inductive effect of substituents around the positively charged group of the dye, thus making the SiC flakes' potential molecular sieves to selectively remove dyes from wastewater. However, Rh6G dye (which features lower steric hindrance than RhB and TBT) revealed an improved adsorption capacity.

Remarkably, the flakes are stable and totally insoluble in water and, even more importantly, they can be easily and fully recycled after each adsorption cycle and reused without affecting the initial adsorption efficiency by a treatment in HNO_3 concentrated solutions, which allows a complete mineralization of the adsorbed dye. Noteworthily, the use of HNO_3 instead of conventional surfactants as SDS removes any further issue regarding the removal of desorbed dye released in the washing solution. Lastly, an early investigation of the photocatalytic properties of SiC flakes was done to study the potentialities of SiC flakes as semiconductive materials for environmental remediation, by coupling adsorbent properties to photocatalytic behavior of SiC.

Data availability

The data supporting this article have been included as part of the ESI.†

Author contributions

M. B.: conceptualization, investigation, methodology, data curation, writing – original draft, formal analysis, writing – review and editing. V. S.: conceptualization, investigation, methodology, data curation, writing – original draft, formal analysis, writing – review and editing. R. F.: investigation, methodology, data curation, formal analysis, writing – review, and editing. S. S.: investigation, methodology, data curation, formal analysis, writing – review, and editing. T. D.:

conceptualization, investigation, methodology, writing – review and editing, supervision, project administration, resources. G. G.: conceptualization, investigation, methodology, writing – review and editing, supervision, project administration, resources. M. E. F.: conceptualization, investigation, methodology, data curation, writing – original draft, writing – review and editing, supervision, project administration, resources, funding acquisition.

Conflicts of interest

There are no conflicts to declare.

Acknowledgements

The authors gratefully acknowledge the financial support by NextGeneration EU funds, through the MUR-PNRR project SAMOTHRACE – SiciliAn MicronanOTecH Research And Innovation CEnter (Project number ECS 00000022). The authors thank Prof. Malandrino Graziella and Dr Lo Presti Francesca for the XRD measurement.

References

1 J. Camacho-Otero, C. Boks and I. N. Pettersen, *Sustainability*, 2018, **10**, 2758.
2 T. Ohji and M. Fukushima, *Int. Mater. Rev.*, 2012, **57**, 115–131.
3 R. Roque-Malherbe, W. Del Valle, F. Marquez, J. Duconge and M. F. A. Goosen, *Sep. Sci. Technol.*, 2006, **41**, 73–96.
4 E. P. Simonenko, A. V. Derbenev, N. P. Simonenko, E. K. Papynov, V. Y. Maiorov, E. A. Gridasova, V. A. Avramenko, V. G. Sevastyanov and N. T. Kuznetsov, *Russ. J. Inorg. Chem.*, 2017, **62**, 863–869.
5 K. A. Salman, Z. Hassan and K. Omar, *Int. J. Electrochem. Sci.*, 2012, **7**, 376–386.
6 P. Singh, S. N. Sharma and N. M. Ravindra, *JOM*, 2010, **62**, 15–24.
7 U. M. Nayef, H. T. Hussein and A. M. Abdul Hussien, *Optik*, 2018, **172**, 1134–1139.
8 B. Lellis, C. Z. Fávaro-Polonio, J. A. Pamphile and J. C. Polonio, *Biotechnol. Res. Innov.*, 2019, **3**, 275–290.
9 P. Parthasarathy, S. Sajjad, J. Saleem, M. Alherbawi and G. McKay, *Separations*, 2022, **9**, 139.
10 I. T. Horváth, Green and Sustainable Chemistry, in *Advanced Green Chemistry*, World Scientific, Hackensack, USA, 2020, ch. 1, pp. 1–15.
11 A. Enesca and L. Andronic, *Nanomaterials*, 2020, **10**, 1766.
12 G. A. Ismail and H. Sakai, *Chemosphere*, 2022, **291**, 132906.
13 M. T. A. Iapichino, R. Fiorenza, V. Patamia, G. Floresta, A. Gulino, M. Condorelli, G. Impellizzeri, G. Compagnini and S. Sciré, *Catal. Commun.*, 2024, **187**, 106850.
14 T. Wang, B. Tian, B. Han, D. Ma, M. Sun, A. Hanif, D. Xia and J. Shang, *Energy Environ. Mater.*, 2022, **5**, 711–730.
15 G. Gautier, J. Biscarrat, D. Valente, T. Defforge, A. Gary and F. Cayrel, *J. Electrochem. Soc.*, 2013, **160**, D372–D379.
16 J. F. Moulder, W. F. Stickle, P. E. Sobol and K. D. Bomben, *Handbook of X-Ray Photoelectron Spectroscopy*, 1992.
17 W. M. K. Raymund, *XPSPeak (Revision) 4.1*, 2000.
18 Y. Shishkin, Y. Ke, R. P. Devaty and W. J. Choyke, *Mater. Sci. Forum*, 2005, **483–485**, 251–256.
19 S. Zangooie and H. Arwin, *J. Electrochem. Soc.*, 2001, **148**, G297.
20 Y. Ke, C. Moisson, S. Gaan, R. M. Feenstra, R. P. Devaty and W. J. Choyke, *Mater. Sci. Forum*, 2006, **527–529**, 743–746.
21 Y. Ke, R. P. Devaty and W. J. Choyke, *Phys. Status Solidi B*, 2008, **245**, 1396–1403.
22 G. Gautier, F. Cayrel, M. Capelle, J. Billoué, X. Song and J. F. Michaud, *Nanoscale Res. Lett.*, 2012, **7**, 2–22.
23 P. Newby, J. M. Bluet, V. Aimez, L. G. Fréchette and V. Lysenko, *Phys. Status Solidi C*, 2011, **8**, 1950–1953.
24 H. Deng, K. Endo and K. Yamamura, *Sci. Rep.*, 2015, **5**(1), 1–6.
25 C. Vecchio, S. Sonde, C. Bongiorno, M. Rambach, R. Yakimova, V. Raineri and F. Giannazzo, *Nanoscale Res. Lett.*, 2011, **6**, 269.
26 I. Kusunoki and Y. Igari, *Appl. Surf. Sci.*, 1992, **59**, 95–104.
27 X. Chen, X. Wang and D. Fang, *Fullerenes, Nanotub. Carbon Nanostruct.*, 2020, **28**, 1048–1058.
28 J. J. Senkevich, C. J. Mitchell, G. R. Yang and T. M. Lu, *Langmuir*, 2002, **18**, 1587–1594.
29 G. D. Sorarù, G. D'Andrea and A. Glisenti, *Mater. Lett.*, 1996, **27**, 1–5.
30 A. Ekoué, O. Renault, T. Billon, L. Di Cioccio and G. Guillot, *Mater. Sci. Forum*, 2003, **433–436**, 555–558.
31 S. Takamoto, T. Yamasaki, T. Ohno, C. Kaneta, A. Hatano and S. Izumi, *J. Appl. Phys.*, 2018, **123**(18), DOI: **10.1063/1.5028273**.
32 C. D. Frye, D. Funaro, A. M. Conway, D. L. Hall, P. V. Grivickas, M. Bora and L. F. Voss, *J. Vac. Sci. Technol., A*, 2021, **39**, 13203.
33 H. Watanabe, T. Hosoi, T. Kirino, Y. Kagei, Y. Uenishi, A. Chanthaphan, A. Yoshigoe, Y. Teraoka and T. Shimura, *Appl. Phys. Lett.*, 2011, **99**(2), DOI: **10.1063/1.3610487**.
34 R. Tu, C. Liu, Q. Xu, K. Liu, Q. Li, X. Zhang, M. L. Kosinova, T. Goto and S. Zhang, *Coatings*, 2022, **12**, 329.
35 A. Arora, A. Pandey, A. Patel, S. Dalal, B. S. Yadav, A. Goyal, R. Raman, O. P. Thakur and R. Tyagi, *J. Mater. Sci.: Mater. Electron.*, 2020, **31**, 16343–16351.
36 M. Thommes, K. Kaneko, A. V. Neimark, J. P. Olivier, F. Rodriguez-Reinoso, J. Rouquerol and K. S. W. Sing, *Pure Appl. Chem.*, 2015, **87**, 1051–1069.
37 K. W. Park and O. Y. Kwon, *Sci. Technol. Adv. Mater.*, 2019, **20**, 599.
38 E. P. Simonenko, A. V. Derbenev, N. P. Simonenko, E. K. Papynov, V. Y. Maiorov, E. A. Gridasova, V. A. Avramenko, V. G. Sevastyanov and N. T. Kuznetsov, *Russ. J. Inorg. Chem.*, 2017, **62**, 863–869.
39 F. K. Van Dijen and E. Mayer, *J. Eur. Ceram. Soc.*, 1996, **16**, 413–420.
40 Y. Yang, K. Yang, Z. M. Lin and J. T. Li, *Mater. Lett.*, 2007, **61**, 671–676.

41 S. Kalam, S. A. Abu-Khamsin, M. S. Kamal and S. Patil, *ACS Omega*, 2021, **6**, 32342–32348.
42 A. Abin-Bazaine, A. C. Trujillo, M. Olmos-Marquez, Adsorption Isotherms: Enlightenment of the Phenomenon of Adsorption, in *Wastewater Treatment*, ed. M. Ince, O. Kaplan Ince, IntechOpen, London, UK, 2022, ch. 1, pp. 1–10.
43 T. S. Khayyun and A. H. Mseer, *Appl. Water Sci.*, 2019, **9**, 1–8.
44 F. O. Okeola and E. O. Odebunmi, *Adv. Environ. Biol.*, 2010, 329–336.
45 V. Vadivelan and K. Vasanth Kumar, *J. Colloid Interface Sci.*, 2005, **286**, 90–100.
46 Y. Kaneko and K. S. Lackner, *Phys. Chem. Chem. Phys.*, 2022, **24**, 14763–14771.
47 M. Vigdorowitsch, A. Pchelintsev, L. Tsygankova and E. Tanygina, *Appl. Sci.*, 2021, **11**, 8078.
48 X. He, K. B. Male, P. N. Nesterenko, D. Brabazon, B. Paull and J. H. T. Luong, *ACS Appl. Mater. Interfaces*, 2013, **5**, 8796–8804.
49 L. Aboutorabi, A. Morsali, E. Tahmasebi and O. Büyükgüngor, *Inorg. Chem.*, 2016, **55**, 5507–5513.
50 J. A. Mason, K. Sumida, Z. R. Herm, R. Krishna and J. R. Long, *Energy Environ. Sci.*, 2011, **4**, 3030–3040.
51 J. P. Simonin, *Chem. Eng. J.*, 2016, **300**, 254–263.
52 L. Chen and B. Bai, *Ind. Eng. Chem. Res.*, 2013, **52**, 15568–15577.
53 W. J. Weber Jr and J. C. Morris, *J. Sanit. Eng. Div.*, 1963, **89**, 31–59.
54 M. Bejblová, D. Procházková and J. Čejka, *ChemSusChem*, 2009, **2**, 486–499.
55 P. Löwenberg, *J. Appl. Chem.*, 1959, **9**, 417–420.
56 R. G. Sandberg, G. H. Henderson, R. D. White and E. M. Eyring, *J. Phys. Chem.*, 1972, **76**, 4023–4025.
57 U. R. K. Lagudu, S. Isono, S. Krishnan and S. V. Babu, *Colloids Surf. A Physicochem. Eng. Asp.*, 2014, **445**, 119–127.
58 L. S. Čerović, S. K. Milonjić, M. B. Todorović, M. I. Trtanj, Y. S. Pogozhev, Y. Blagoveschenskii and E. A. Levashov, *Colloids Surf. A Physicochem. Eng. Asp.*, 2007, **297**, 1–6.
59 R. Gong, H. Song, J. Yang and H. Liu, *Acad. J. Sci. Technol.*, 2023, **5**, 158–162.
60 J. Hedlund, M. S. Nobandegani and L. Yu, *J. Membr. Sci.*, 2022, **641**, 119893.
61 M. G. Kim, J. E. Lee, K. S. Kim, J. M. Kang, J. H. Lee, K. H. Kim, M. Cho and S. G. Lee, *New J. Chem.*, 2021, **45**, 3485–3497.
62 S. Xia, L. Zhang, G. Pan, P. Qian and Z. Ni, *Phys. Chem. Chem. Phys.*, 2015, **17**, 5345–5351.
63 P. Eswaran, P. D. Madasamy, K. Pillay and H. Brink, *Biomass Convers. Biorefin.*, 2024, **2024**, 1–21.
64 G.-M. Zeng, X. Li, J.-H. Huang, C. Zhang, C.-F. Zhou, J. Niu, L.-J. Shi, S.-B. He and F. Li, *J. Hazard. Mater.*, 2011, **185**, 1304–1310.
65 L. Masse, J. Puig-Bargués, M. Mondor, L. Deschênes and G. Talbot, *Sep. Sci. Technol.*, 2015, **50**(16), DOI: **10.1080/01496395.2015.1062395**.
66 M. Gaeta, M. Barcellona, R. Purrello, M. E. Fragalà and A. D'Urso, *Chem. Eng. J.*, 2022, **433**, 133262.
67 W. C. Holmes and B. W. French, *Stain Technol.*, 1926, **1**, 17–26.
68 Z. Zaheer, W. A. Bawazir, H. Alwael, F. M. Al-Jefri and M. Salem, *J. Mol. Liq.*, 2024, **394**, 123794.
69 O. Impert, A. Katafias, P. Kita, A. Mills, A. Pietkiewicz-Graczyk and G. Wrzeszcz, *Dalton Trans.*, 2003, **3**, 348–353.
70 S. M. Ghoreishian, K. Badii, M. Norouzi, A. Rashidi, M. Montazer, M. Sadeghi and M. Vafaee, *J. Taiwan Inst. Chem. Eng.*, 2014, **45**, 2436–2446.
71 M. O. Fatehah, H. A. Aziz and S. Stoll, *J. Colloid Sci. Biotechnol.*, 2014, **3**, 75–84.
72 P. L. Waalewijn-Kool, M. Diez Ortiz, N. M. Van Straalen and C. A. M. Van Gestel, *Environ. Pollut.*, 2013, **178**, 59–64.
73 G. R. Wiese and T. W. Healy, *J. Colloid Interface Sci.*, 1975, **52**, 452–457.

